Real-Time and High-Resolution Monitoring of Neuronal Electrical Activity and pH Variations Based on the Co-Integration of Nanoelectrodes and Chem-FinFETs

Luca Bettamin, Fabrice Mathieu, Florent H Marty, Marie Charline Blatche, Daniel Gonzalez-dunia, Elsa Suberbielle, Guilhem Larrieu

RESEARCH ARTICLE

NANO · MICRO small
www.small-journal.com

Real-Time and High-Resolution Monitoring of Neuronal Electrical Activity and pH Variations Based on the Co-Integration of Nanoelectrodes and Chem-FinFETs

*Luca Bettamin, Fabrice Mathieu, Florent H. Marty, Marie Charline Blatche, Daniel Gonzalez-Dunia, Elsa Suberbielle, and Guilhem Larrieu**

Developing new approaches amenable to the measurement of neuronal physiology in real-time is a very active field of investigation, as it will offer improved methods to assess the impact of diverse insults on neuronal homeostasis. Here, the development of an in vitro bio platform is reported which can record the electrical activity of cultured primary rat cortical neurons with extreme sensitivity, while simultaneously tracking the localized changes in the pH of the culture medium. This bio platform features passive vertical nanoprobes with ultra-high signal resolution (several mV amplitude ranges) and Chem-FinFETs (pH sensitivity of sub-0.1 pH units), covering an area as little as a neuronal soma. These multi-sensing units are arranged in an array to probe both chemically and electrically an equivalent surface of ≈ 0.5 mm^2. A homemade setup is also developed which allows recording of multiplexed data in real-time (10 ps range) from the active chem-sensors and passive electrodes and which is used to operate the platform. Finally, a proof-of-concept is presented for a neuro-relevant application, by investigating the effect on neuronal activity of Amyloid beta oligomers, the main toxic peptide in Alzheimer's Disease, which reveals that exposure to amyloid beta oligomers modify the amplitude, but not the frequency, of neuronal firing, without any detectable changes in pH values along this process.

1. Introduction

One of the major challenges in modern electrophysiology lies in understanding how neuronal cells communicate under normal and pathological conditions. This type of investigation remains challenging, mainly because of the difficulties to have continuous access to neuronal functioning over long periods of time. The difficulties are multiple, because even if neurons are individual cells, they function as a network regulated by multiple incoming and outgoing exchanges with neighboring cells. Thus, their monitoring requires measures at the cellular level, whilst being multiplexed at the network level. Traditionally, the main physical feature being monitored is electrical activity, since communication between these excitable cells is governed by very fast voltage pulses (ms). Direct measurements using microelectrode arrays,[1–3] (MEA) or indirect measurements through calcium imaging[4] (CI) both allow monitoring the electrical signals at the cell network level. Both are, however, limited in temporal resolution (CI), signal resolution (MEA, CI), or even spatial resolution, unless using very complex or expensive equipment such as two-photon imaging[5,6] or high-density MEA.[7] Moreover, the concomitant measure of additional parameters, such as local variations in diverse chemical species (ions, neurotransmitters, etc.), could also be of great interest to better understand the pathophysiology of neurological diseases. Indeed, electrical and chemical parameters are often intimately linked[8,9] and the ability to monitor these physical quantities in parallel could favor decisive advances in the understanding of neuronal systems. For example, the possibility to monitor pH levels, both in specific locations and at the global scale could help to understand the pH oscillations during brain activity.[10,11] Indeed, increased neuronal activity can produce large ion fluxes and localized acidosis might influence the activation or inhibition of ion channels and receptors.[12] To achieve such an endeavor and to propose improvement of the currently available systems, the sensors should be small to allow measurements at the cellular scale. They should also favor tight interaction with neurons to increase the resolution level. In this sense, 3D nanostructured

L. Bettamin, F. Mathieu, M. C. Blatche, G. Larrieu
LAAS-CNRS
CNRS
Université de Toulouse
Toulouse 31031, France
E-mail: glarrieu@laas.fr
L. Bettamin, F. H. Marty, D. Gonzalez-Dunia, E. Suberbielle
INFINITY
INSERM
CNRS
Université de Toulouse
Toulouse 31031, France

The ORCID identification number(s) for the author(s) of this article can be found under https://doi.org/10.1002/smll.202309055

DOI: 10.1002/smll.202309055

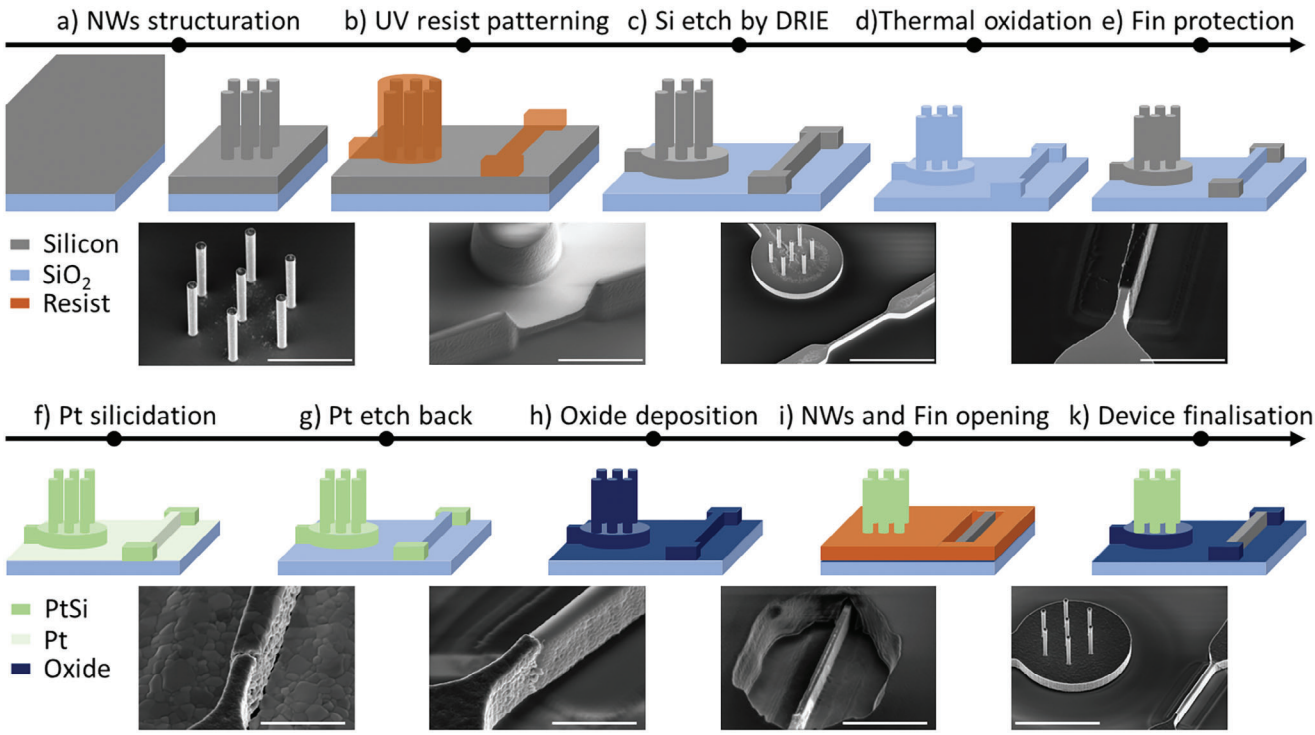

Figure 1. Schematic view of the step-by-step process to build the nanoelectrodes and nanotransistors array. a) Top-down structuration of the vertical silicon NWs (Scheme (top) and SEM image(bottom) of the NWs. Scale bar: 4μm). b) Photolithography resist patterning to transfer the electrode and fin-like geometry on the surface (Scheme (top) and SEM image (bottom) of the developed photoresist. Scale bar: 10 μm). c) Silicon plasma etching down to the BOx layer (Scheme (top) and SEM image (bottom) of the silicon structuration. Scale bar: 10 μm). d) Thermal oxidation. e) Fin oxide layer structuration (Scheme (top) and SEM image (bottom) of the transistor channel. Scale bar: 2 μm). f) Formation of the PtSi silicide metallic layer (Scheme (top) and SEM image (bottom). Scale bar: 1 μm). g) Unreacted platinum chemically etch back (Scheme (top) and SEM image (bottom). Scale bar: 1 μm). h) Oxide layers deposition; i) Resist structuration for NWs and fin opening (Scheme (top) and SEM image (bottom)of the exposed fin channel. Scale bar: 3 μm). k) Overview of the resulting device (Scheme (top) and SEM image (bottom). Scale bar: 5 μm).

microelectrodes [13–16] have emerged as very well-suited systems, by offering a miniaturization of the detection surface. In other settings, higher resolutions of measured signals have been obtained by penetrating the cell by local perforation of the membrane (electroporation, optoporation, etc.)[14,17–21], they, however, have an impact on cell viability and limit recordings in the long term. Recently, it has been shown that high resolution can be reached intrinsically without manipulation of the membrane, using new nanoelectrode arrays (NEA)-based devices.[22–25] Nevertheless, to date, there is no in vitro platform allowing high-resolution multi-physics detection at the cellular level. In this work, we propose the co-integration of two types of 3D nanodevices, namely passive nanoprobes, and active nano transistors, which allow to sense and record in real-time electrical activity and local chemical variations down to a single-cell resolution within neuronal networks. After extensively describing the processing of the silicon-based technology to enable the co-integration of the devices at large scale, we provide a detailed characterization of the properties of the two types of recording devices and demonstrate their advantages relative to the current state-of-the-art. Finally, we show, as a proof-of-concept, that this setup allows precise recordings of neuronal activity, as illustrated when assessing the impact of amyloid beta oligomers, the main toxic peptide in Alzheimer's Disease, on neuronal network communication.

2. Results and Discussion

2.1. Device fabrication

The combination of the two types of sensors (nano-probes, nano-transistors) was achieved by combining conventional micro/nano-electronic steps on the scale of a whole substrate, including conventional lithography, deep reactive ion etching (DRIE), thermal oxidation, and metal or oxide depositions (**Figure 1**). Starting with a 4″ silicon on insulator (SOI) wafer (4 μm-thick active Si(100) layer per 1 μm-thick buried silicon dioxide – BOx per 400 μm-thick bulk silicon), a first step was dedicated to the structuration of the vertical nanowires. A photolithography step was performed with an i-line stepper (Canon) to obtain resist nanodots with a diameter of 450 nm. The patterns were next transferred to the active Si layer using an anisotropic plasma etching step, by deep reactive ion etching. Vertical etched nanopillars of 3.5 μm-height (Figure 1a) were obtained with an excellent vertical profile, a very smooth surface, and a high surface-to-volume ratio (H/S ≈ 8). The remaining active Si layer (≈500 nm) was structured by second photolithography to design the active channel of the transistors, the access lines to the nanoprobes, the source/drain contacts of the transistors, and the external contact pads on the wafer (Figure 1b). Again, an anisotropic plasma etch was used to define the structures in the remaining silicon layer,

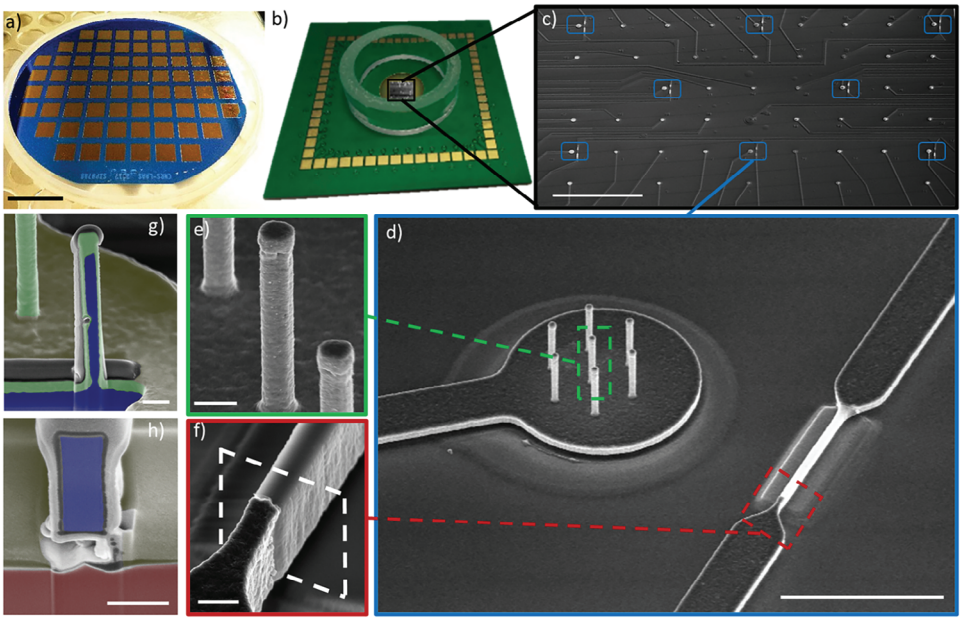

Figure 2. Macroscopic and scanning electron microscopy views of the final devices. a) Photograph of the 4" wafer after fabrication in the clean room. A single wafer was used to produce up to 68 devices. Scale bar: 2 cm. b) Photograph of the complete device, including the packaging of the chip with a PCB compatible with commercial standards (MCS configuration) and a glass well for the culture medium. c to h) SEM images of the chip electrode array and its nanoelectrodes. Panels d to h) show enlarged views outlined by the different colored boxes. c) The recording sites of each device are composed of 47 passive nanoelectrodes, with 8 of them coupled with active Chem FinFETs to form a multi-sensing unit. The spacing between each passive nanoprobe is 100 µm. Scale bar: 200 µm. d) Enlarged view of the cointegration of the active and passive devices forming a multi-sensing unit. Scale bar: 10 µm. e) Details of one passive nanoprobe. The PtSi surface (in green) is shown after the annealing process. f) Detail of the finFET channel, transition between PtSi source and gate oxide. g) Focused ion beam (FIB) cross-section of a nanoprobe, where it is possible to distinguish the different layers of doped silicon (blue) and PtSi (green) and insulator layers (yellow). h) Focused Ion Beam (FIB) cross-section of a finFET channel, the fin (blue), the BOx (red), and the insulator layer (yellow). Scale bars for e–h: 500 nm.

reaching the buried oxide (BOx) to guarantee electrical insulation between the conductive elements of each device (Figure 1c). The active channel of the transistor is a 3D fin-shaped nanostructure with a width of ≈400 nm and a height of ≈600 nm. The distance between the nanoprobe and the transistor was set at 10 µm, corresponding to the size range of a neural soma, forming a multi-sensing unit. Then, the size of the obtained structures (diameter of the nanopillars, width of the fins) was tuned using a sacrificial thermal oxidation, to consume the silicon layer at the sample surface. A wet oxidation (850 °C per 60 min) was performed to create an 85 nm-thick SiO_2 layer on bulk (100) Si. Each resulting electrode had a set of 3 or 7 nanopillars, with a pitch of 2 µm between each nanostructure. The electrodes in the array were spaced by 100 µm (**Figure** 2c). The fin channel dimensions (Figure 2h) were 500 nm high and 218 nm wide. The sacrificial oxide was removed by chemical buffered oxide etch (BOE) on the entire wafer, except for the channel fin of the transistor (Figure 1e), protected by a photoresist with a third photolithography step. The diameter of the nanopillars was reduced to 300 nm (H/S ≈ 12) after the chemical etching of the sacrificial oxide around the nanowires. An ion implantation step (boron) with thermal dopant activation was performed to create highly doped source-drain regions (1.10^{20} atoms cm^{-3}) in the active devices. The implantation conditions (energy) were tuned to confine the dopant in the remaining oxide layer covering the transistor channel, in order to let the channel free of dopant. Note that nanoprobes and access lines were also doped at the same time during this step, thereby reducing the sheet resistance of these conductive tracks. The next step consisted of the conversion of the silicon surfaces present on the sample into a platinum silicide, allowing a gain at different levels, notably: i) a better interface impedance for the nano-probes, ii) a lower source/drain contact resistance for the transistors, and iii) an improved conductivity of the access lines. To this aim, an 80 nm Pt layer was first anisotropically deposited by physical vapor deposition (PVD), followed by rapid thermal annealing (RTA) at 500 °C to create the PtSi silicide layer (Figure 1f). The reaction of Pt solicitation occurred only where the Pt layer was in contact with the silicon on the non-oxidized surfaces. Therefore, a selective chemical etch (diluted aqua regia) allowed removing the excess of non-reacted platinum on oxide, leaving only the silicide part (Figure 2f). The obtained PtSi layer was uniform around the vertical nanopillars as well as the device access lines (Figure 2e,g). Then, the access lines were metalized with aluminum up to the external pads, dedicated to the bounding with the external printed cardboard. Finally, to insulate the device for its use in a liquid medium, the deposition of an oxide bi-layer was performed. To improve the stability of the device for a long period in liquid, a first layer of 50 nm alumina (Al_2O_3) was added by atomic layer deposition (ALD) and seconded by a layer of 200 nm silicon oxide added by plasma-enhanced chemical vapor deposition. Last, the active region of the two sensors was specifically addressed. The oxide layers on the fin channel of the transistors were chemically etched (BOE) using a localized opening in a thick resist layer (Figure 1i). A 5 nm-thin Al_2O_3 layer was deposited by ALD to

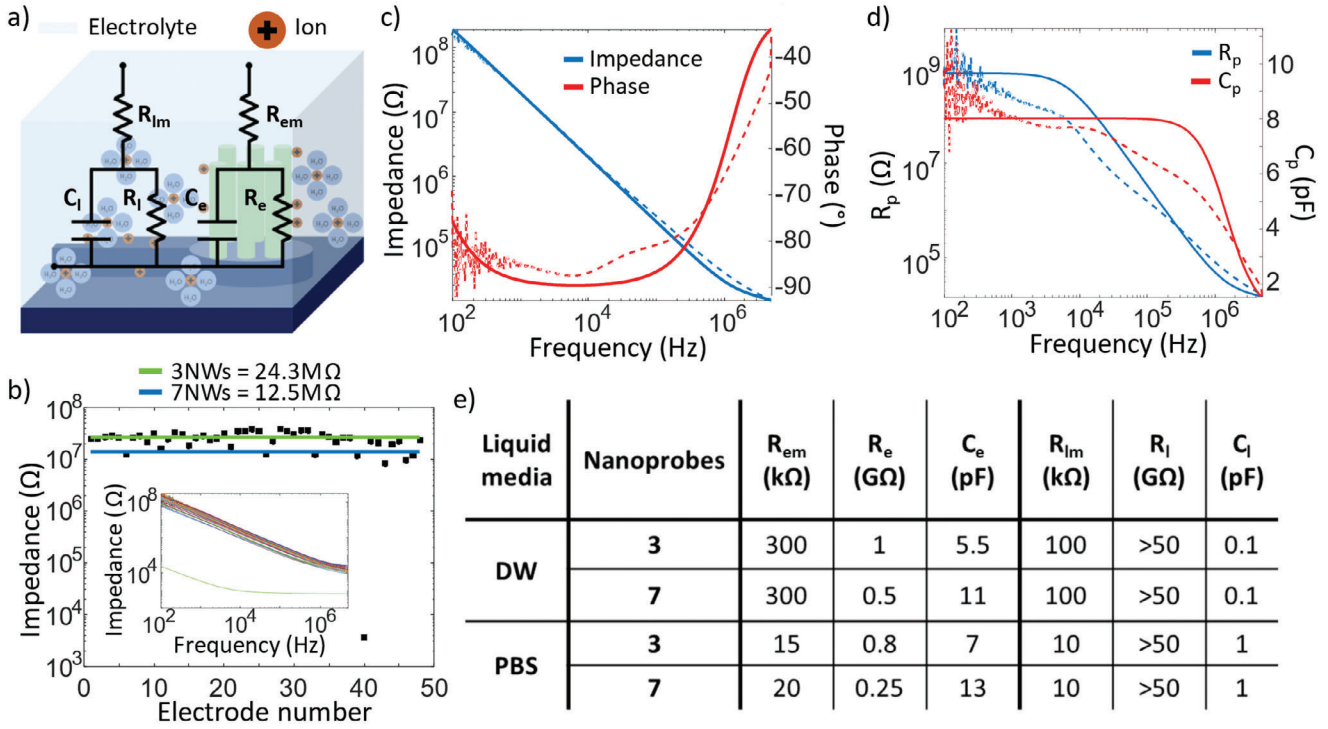

Liquid media	Nanoprobes	R_{em} (kΩ)	R_e (GΩ)	C_e (pF)	R_{Im} (kΩ)	R_I (GΩ)	C_I (pF)
DW	3	300	1	5.5	100	>50	0.1
	7	300	0.5	11	100	>50	0.1
PBS	3	15	0.8	7	10	>50	1
	7	20	0.25	13	10	>50	1

Figure 3. Electrochemical impedance spectroscopy (EIS) characterization of the nanoelectrodes with analytical electrical model. a) Schematic view of the equivalent circuit model (superposed in black) used to simulate the system. R_{Im}, R_I, and C_I are used to describe the conductive line-medium interface. R_{em}, R_e, and C_e are used to describe the electrode-medium interface b) The value of impedance was measured for each passive electrode on the device. A clear trend differentiates the impedance value at 1 kHz for electrodes with 3 versus 7 nanoprobes coherently with the different surface areas. The insert on the top of the panel shows the measured value of the EIS impedances for each electrode on the device. c) Graph showing the measured (dashed lines) and simulated (bold lines) impedance (blue) and phase (red) of the nanoelectrodes, as a function of the signal frequency, d) Graph showing the parallel resistance (R_p in blue) and capacitance (C_p in red) behavior of the system. e) Representative table of each element value of the electrical equivalent model extracted for different conditions fitting the measures.

create the liquid gate insulator layer of the FinFETs. This chosen material is known for its great quality as a dielectric-sensitive layer in ISFET technology.[26,27] Finally, a thin resist layer was used to cover the transistor device and the electrode of the nano-probe, allowing the selective etch of the isolating layer covering the metallic surface of the nanoprobes (Figure 2d,e).

The micro/nanofabrication at the wafer scale led to 68 identical chips (Figure 2a). The wafer was diced in unitary chips. Each chip was bonded by a flip-chip with gold bumps to a Printed Circuit Board (PCB), which displayed external contacts that were designed to be compatible with commercial recording setups (Figure 2b). An underfilled epoxy glue was introduced between the PCB and the Si chip to guarantee electrical insulation between the contact pads and to enhance the mechanical stability of the whole system. Finally, a glass ring was glued with PDMS, to allow the cell culture well to be centered on the active device (Figure 2b). The sensing area was composed of an array of 8 multi-sensing units (coupling a nanoprobe and a FinFET) with a 400 µm pitch (Figure 2d), with a secondary network of 47 nanoprobes with a denser pitch (100 µm). The goal was to allow simultaneous local recordings of electrical activities and pH variations of the medium around neurons, in a distributed manner across the platform surface.

2.2. Characterization of the passive electrodes

To study the passive impedance of the device, an impedance analyzer (Agilent 4294A) was used together with a manual probe station (Signatone CM210) to connect the external contact pads. The measures were taken via electrochemical impedance spectroscopy (EIS) using a two-electrode setup, with a counter electrode and a working electrode. The device was filled with an ionic solution (phosphate-buffered saline, PBS) to simulate the conditions of cell culture. The counter electrode, a platinum electrode, was plunged into the solution and the working electrode was connected to the passive electrode on the device. The measures were taken from electrodes with three or seven nanopillars. An equivalent electrical circuit was proposed to describe the results of the system, based on the Randles' cell, taking into consideration both the electrode/electrolyte interface of the nanopillars and the insulated surface interface along the conductive access lines (**Figure 3a**). Thus, both parts of the circuit were composed of a resistance and a capacitance in parallel, describing the interfaces with the solution for the insulated zones of the device and for the sensitive ones. In series to that basic cell, a resistance represented the medium properties. The impedance values for both three and seven nanopillars were measured specifically at 1 kHz (Figure 3b), resulting in 24.3 MΩ for three nanopillars and 12.5 MΩ

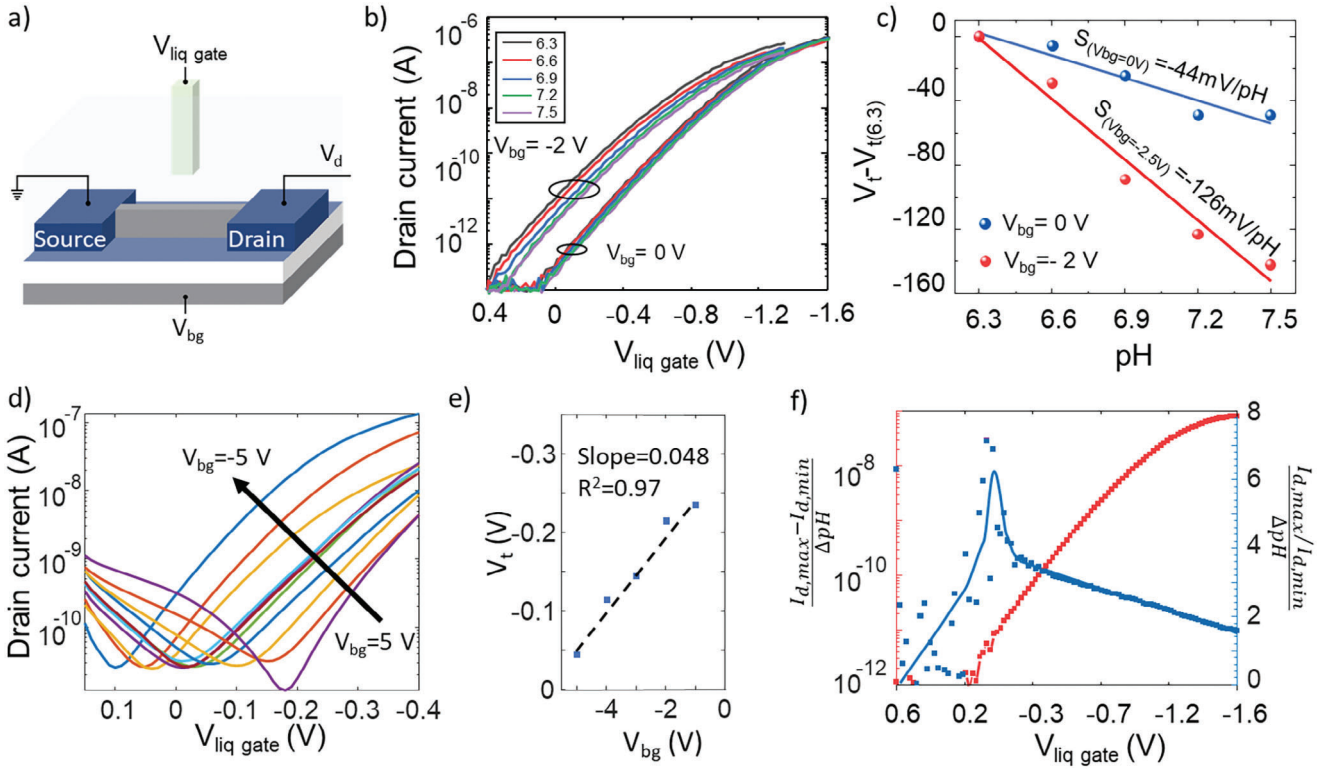

Figure 4. FinFETs electrical characterization with liquid gate. a) Schematic representation of FinFETs structure and contacts. b) Static characteristics of the FinFET (Drain current – Gate voltage: I_{ds}–V_{gs}) in log scale of the drain current at V_d = −0.1 V, without and with back-gate (V_{bg}) polarization of −2 V at pH values of 6.3, 6.6, 6.9, 7.2, and 7.5. c) Nernstian response of the FinFET at 0 V showing −44 mV per pH without back-gate polarization and −126 mV per pH with the back-gate polarization (−2 V), going above the Nernstian limit of pH sensitivity. d) Plot of the FinFET current (I_{ds}) variation with different back-gate polarizations in the function of the polarization (V_{gs}). e) Variation of the transistor threshold voltage (V_t) in the function of the back-gate negative polarization (V_{bg}), showing a linear relationship $V_t = f(V_{bg})$. f) Maximal and minimal current ratio and difference, normalized on the pH step, assessing the device sensitivity and current range on the entire liquid gate voltage range.

for seven nanopillars, which scaled appropriately with the active surface of the nanowires in contact with the solution (8.7 μm^2 for 3 nanowires/20.3 μm^2 for 7 nanowires). Also, the impedance characteristics of the on-chip reference electrode (equivalent surface of 1.5 × 10^6 μm^{-2}) could easily be recognized with its lower value due to the much larger surface. The footprints of the 7- and 3-nanopillar-based electrodes were 12.5 and 3.14 μm^2, respectively. Because the entire equivalent surface of the electrode was held at the same potential, the detection of cellular electrical activity was performed on a significantly smaller footprint compared to conventional planar electrodes (which have a footprint of ≈900 μm^2, or even larger). Consequently, the 7-nanopillar electrode provided a favorable balance between footprint size and moderate interface impedance. The EIS measurements were fitted with the equivalent electrical circuit model described before. Measured data were in good agreement with the model (Figure 3c,d). Both impedance and phase components could be simulated, as well as the most relevant parallel capacitive and resistive components. Based on an accurate fitting of the experimental data with the model, an evaluation of each element in the equivalent electrical circuit could be extracted (Figure 3e). It showed coherence in the values of the liquid medium (Distilled Water or PBS) for R_{em} and R_{lm}. For the saline medium (PBS), the relative resistance was lower due to the presence of ions in the solution. The resistance and capacitive value of the access lines (R_l and C_l) showed that the insulating layer correctly avoided any major signal leakage, with an impedance larger than 100 GΩ in both cases. The obtained values for the sensing part of the equivalent circuit highlighted a Faradaic behavior of the interface, which is a typical behavior of such a metallic electrode. Besides, the measured impedance of the probes was in the same range as values described in other studies of metallic nanowire-based electrodes,[20] taking into account the diversity in materials and geometry of the devices.

2.3. Characterization of the ChemFET device

we next evaluated the sensitivity of the FinFET device to the variation of its chemical environment (namely pH). In principle, the device should be able to monitor small variations of pH around the physiological pH of the neuronal culture medium (≈7.2). When conducting characterization in liquid, such as pH testing or neuron electrophysiology, a pH-adjusted Tyrode solution was used (details of composition and protocol can be found in the Experimental Section). The operating diagram of the FinFET device (**Figure 4a**) was as follows: the transistor was biased by a voltage on the drain (V_d), the source being grounded. The gate

bias was applied in the liquid (V_{liqgat}) through an external Pt electrode. Finally, a contact on the back side allowed an additional modulation of the conduction of the transistor channel by the gate bias induced by the buried oxide of the SOI. The $I_{ds} - V_{liqgat}$ characteristics were obtained with a parameter analyzer (Agilent 4156C). The static characteristics (Figure 4b) showed an excellent response as a function of the liquid gate potential with an I_{on}/I_{off} dynamic of 6 decades, a very low off-state current (≈pA), and a very low gate voltage range (V_g@ON-V_g@OFF 1.2 V) thanks to an extremely abrupt sub-threshold switching. It is interesting to note that these performances were obtained at a very low bias voltage V_{ds} (−0.1 V), thereby allowing a lesser solicitation of the device, notably less self-heating, which may considerably reduce any potential impact on the long-term degradation, or interference with the biological material being probed (neuronal cells). The transistor response to five different pH-adjusted Tyrode solutions from 6.3 to 7.5 with a step of 0.3 pH units is shown in Figure 4b. The extracted value of the threshold voltage as a function of the pH value (Figure 4c) displayed a Nernstian response (44mV per pH). This range of sensitivity was comparable to other devices described in the literature that integrate an Al_2O_3 liquid gate oxide layer.[28] Moreover, our system offered another level to modulate the current variation in the 3D channels, allowed by its back-gate structure (bulk substrate/buried oxide). Figure 4e presents the effect of the back-gate polarization from 5 to −5 V, with $V_{ds} = -0.1$ V, shifting the threshold voltage value from 0.34 to 0.05 V. The FinFET response to the pH was evaluated with a back gate voltage fixed at −2 V (Figure 4b) and displayed a drastic gain of sensitivity. The Nernstian response of the device shifted from 44 mV per pH, without the back-gate polarization, to 126 mV per pH, with a back-gate polarization of −2 V (Figure 4c), which was above the theoretical Nernstian limit.[29,30] The gate system could be schematically divided into two parts: i) capacitance from the liquid gate ($C_{liqgat)}$, which could be approximated to the Al_2O_3 layer contribution, and ii) the capacitance from the back gate (C_{bg}). Based on the voltage divider, the gate coupling ratio C_{liqgat}/C_{bg} was proportional to $\Delta V_{liqgat}/\Delta V_{bg}$, which could be nicely extracted from Figure 4e. The smaller C_{bg} compared to the C_{liqgat} was able to amplify the sensitivity to pH change largely over the theoretical Nernst limit.[29] In order to evaluate the sensitivity with other figures of merit, we assessed the ratio between the maximal and minimal current, normalized for unity of pH step, giving a measure of the device sensitivity along the whole liquid gate polarization range (Figure 4f). In addition, the difference between maximal and minimal current, normalized on the unity of the pH step, was plotted in the same graph. A high current range (>nA) is of prime importance to allow very precise monitoring in real-time, even if the relative sensitivity may not be at its peak value.

2.4. Real-time recording setup

The recording platform was a homemade system that also integrated several commercial modules. It allowed the simultaneous monitoring of both electrical and chemical variations from active and passive sensor devices in real-time and in a multiplexed way. As shown in **Figure 5**a, it was composed of a commercial MEA holder (MEA1060-Inv-BC from Multichannel System for a 60-channel MEA), a home-made electronic card (MultisensONE) where the electronics to manage the system (recording, stimulation, and filtering) were integrated with a multichannel data acquisition card (USB 6363, a 16-bit ADC, 16 channels from National Instruments), which converted the analog data into digital values and was driven by a home-made software (GenAcq). The multi-physics device with cultured cells was positioned inside the MEA holder in a humidified incubator set at 37 °C and 5% CO_2. It was connected by a SCSI cable to the MultisensONE multiplexer (shown in Figure 5a), a homemade electronic card. The multiplexer allowed to direct each one of the 60 inputs to one of 5 alternatives, schematically represented in Figure 5a: ground, DC polarization (i.e., to polarize the drain of the transistor, V_d), AC polarization (i.e., for cell electroporation V_{ep}), potential measure (i.e., for nanoprobe monitoring) or current measure (i.e., for monitoring the current variation in the transistor). The whole setup was also electrically connected to a common ground and a computer, through a USB connection. The recording setup was controlled by a homemade software (GenAcq) developed on LabVIEW that allowed following in real-time the characteristics of the transistors and the nanoprobes, to execute live data treatment and save the data. For each experiment, primary cultures of rat cortical neurons (refer to the experimental section for specific details regarding cell preparation) were plated on the multi-sensing device. Neuronal concentration was adjusted in order to be plated onto the chips at a density of 120 000 cells cm^{-2}. The devices were prepared in advance by sterilization with ethanol at 70% for at least 20 min, coating with a solution of 0.5 mg ml^{-1} poly-ornithine (Sigma) for at least 6 h, followed by an additional coating using laminin (5 µg ml^{-1}, Thermo Scientific) for at least 4 h prior to the plating.[31] Once plated on the devices, cultures were kept at 37 °C, 5% CO_2, in a humidified incubator for at least 10 days in vitro (DIV) prior to the first electrophysiological recordings, although we typically kept neurons in culture until 15 DIV, to allow them to reach electrical maturity and full connectivity.[32] The culture medium was renewed by half at DIV 3 and DIV 7 with glial cell-conditioned culture medium (refer to the experimental section for specific details regarding conditioned culture medium preparation) in order to increase viability of the neuronal cultures. These conditions allowed to have long lasting primary cell cultures of neurons for up to one month. For these long-term cultures, excessive evaporation was monitored and compensated when needed.

Neurons grown on the devices were fixed by glutaraldehyde and processed for the generation of high-resolution images using scanning electron microscopy, in order to visualize the interaction between neuronal somas and neurites with the 3D nanosystems. Figure 5b shows a representative image of this analysis. The colored SEM image clearly highlighted the interaction between the cells and the passive and active electrodes of the device, where both vertical nanoprobes and transistor channels were engulfed by neuronal soma, axons, or dendrites. In order to refine the characterization of the interaction of neurons on nanostructures, arrays of 500 nm diameter nanowires with varying pitches were used. Figure 5e shows tilted SEM images of soma on an array with a pitch between nanostructures of 1 and 2 µm, along with FIB sections of these cell bodies to image cell membrane overlap on nanostructures. It appeared that a minimum pitch of 2 µm was required to achieve proper

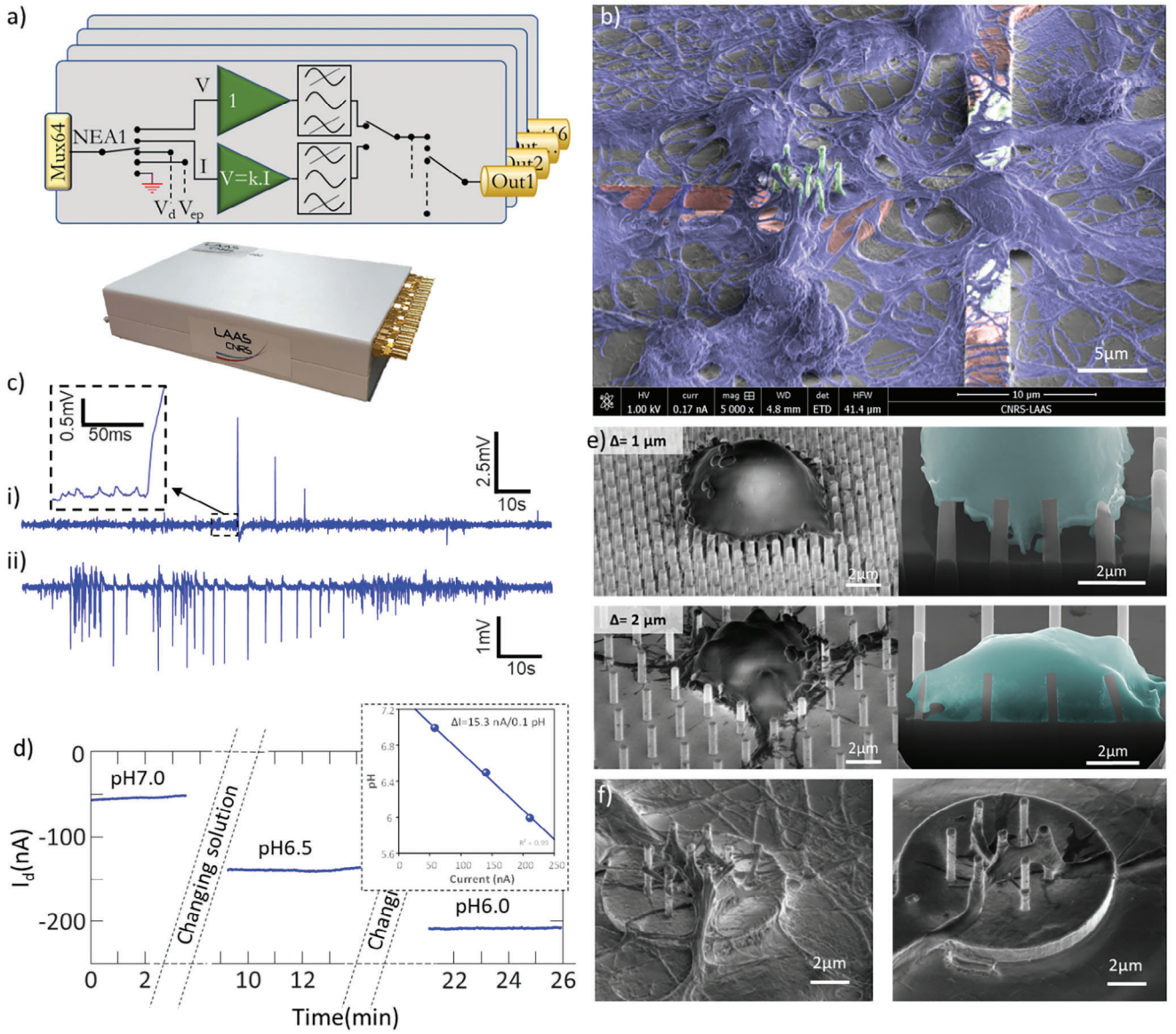

Figure 5. Main components of the recording and examples of its measure capabilities. a) Schematic representation of its internal multiplexing possibility (Ground contact, DC polarization V_d, AC polarization V_{ep}, current measure I, potential measure V) for one contact (NEA1) and external inputs (Mux64) and outputs (Out1, Out2, etc.). b) Pseudo-colored SEM image of primary rat neurons grown on the multi-sensing unit and processed for fixation and staining at 14 days in vitro (DIV). c) Representative examples of electrical activities recorded from two neighboring nanoprobes. i) and ii), of spontaneous recorded activity with high signal-to-noise ratio peaks and in zoom inset, smaller spike activity occurred before the action potential (AP) firing d) Plot showing variations in pH levels monitored in real-time with three different pH solutions. The inset shows the linear variation of the current in the FinFET, as a function of the pH value. e) Tilted SEM images showing cell somas on arrays of nanowires (500 nm diameter) with pitches between nanostructures of 1 µm and 2 µm, accompanied by associated FIB sections of these cell bodies. f) Tilted SEM images displaying neurite extensions around the nanoelectrodes.

engulfment of the soma on the nanoelectrodes. Denser nanowire configurations would induce a top-state configuration, where the interaction with the nanoelectrodes was limited, resulting in a significant increase in seal resistance and, consequently, degradation of signal resolution. The 2 µm pitch drawing rule was applied to design the nanoelectrodes. Additionally, Figure 5f showed that this nanoelectrode configuration was also suitable for the perfect engulfment of the sub-cellular parts of neurons. Next, we conducted an experiment to validate our multi-sensing platform for real-time monitoring. Figure 5c shows an example of spontaneous neuronal activity in Tyrode solution recorded from neurons grown for 15 DIV through 2 different NEAs separated by 100 µm, where high resolution of the spiking activity of the neuronal culture could be detected, with signal-to-noise ratio reaching up to 200. Moreover, several points of importance could be noted: i) the detected peaks could be either negative or positive; ii) the peaks detected by the two neighboring electrodes were not similar, indicating that there was no cross-talk between

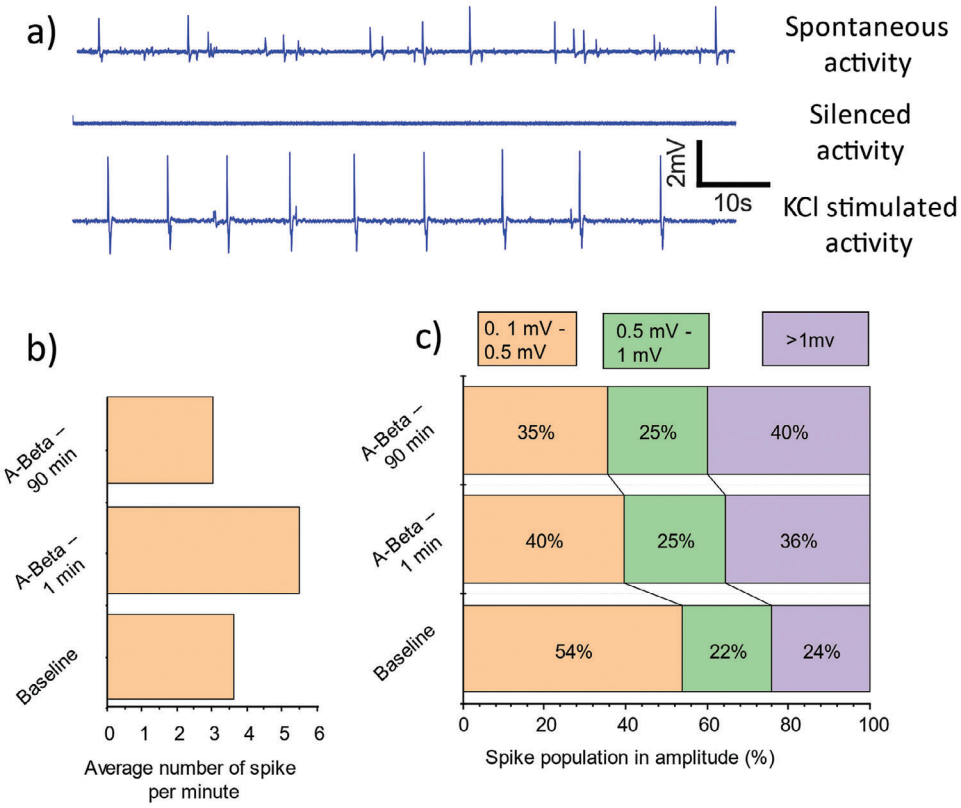

Figure 6. Examples of recordings and applications to biological studies. a) Representative examples of a series of recordings on a primary neuronal rat culture. First is shown spontaneous activity (i.e., in the Tyrode solution without any additive), or baseline, followed by the electrical activity measured after adding a silencing drug cocktail. Neurons were next depolarized using KCl and activity was immediately recorded thereafter. All recordings shown in the figure were sequentially measured from the same electrode. b,c) Bar charts representing the variation of b) the frequency of activation and c) the normalized spike recorded amplitudes upon exposure to Aβ1-42 oligomers. The recordings were done first at baseline in Tyrode solution, next one min after incubation with Aβ1-42 oligomers, and finally 90 min later. Importantly, pH values were monitored simultaneously from the FinFET devices and did not reveal any change in the pH throughout this experiment. The experiment with Aβ1-42 oligomers was repeated twice on a total of four devices. Neurons were plated at a density of 120000 cells cm^{-2}.

them; iii) we observed higher amplitude spikes, which might be due to action potentials fired by neurons in the direct vicinity of the nanopillars electrodes. Finally, we performed a real-time evaluation of pH variations in a range of one pH unit from 6 to 7 using the Chem-FinFETs, as shown in Figure 5d. We observed that the transistor current level varied linearly according to the pH value and was stable in time. Notably, the current variation upon a change of 0.01 pH unit was higher than 1.5 nA (insert of Figure 5d). The current stability of transistors in physiological medium was assessed across different devices, with operational conditions set at $V_{ds} = -0.1V$ and $V_{bg} = -1.5V$. The standard deviation of the measured current was extracted as shown in Figure S1 (Supporting Information) and the results can be found in Table S1 (Supporting Information). The average current noise across all devices was measured at 105 pA. Given the Gaussian nature of the noise, the likelihood of it deviating beyond 3σ from the mean was therefore extremely low. Consequently, we could consider current variations in the transistor exceeding 300 pA as the detection limit for pH variations, which corresponded to a theoretical detection limit of 0.002 pH units. It is, therefore, reasonable to postulate that detections of 0.01 pH units (current variations surpassing 1 nano ampere), as observed in previous studies[33] of neuronal physiological activity, could be reliably captured.

2.5. Use of the device for assessing neuronal responses to diverse stimuli

Primary rat cortical neuronal cultures at 15 DIV were next subjected to different treatments and we assessed the ability of our bio-platform to detect changes in electrophysiological properties of the cultures. The electrical activity of the cell culture was recorded with the passive electrodes and we first measured the spontaneous activity of a 15 DIV culture. The spontaneous and periodic firing activity measured on one electrode was set as the baseline for the subsequent measurements on the same electrode (**Figure 6a**). First, neuronal activity was silenced using a drug cocktail composed of 1 µM Tetrodotoxin (TTX), 20 µM CyanoNitroQuixaline (CNQX), and 50 µM (*2R*)-amino-5-phosphonovaleric acid (APV). These drugs impeded the activation of calcium channels and the function of the AMPA and NMDA glutamatergic receptors present at the synapses. We confirmed that this effect was completely reversible when rinsing

the solution. Indeed, once the drug cocktail was rinsed and neurons had returned to their standard culture medium, the electrical activity returned to baseline levels. The sensitivity of the electrodes was also proven upon chemical stimulation of neuronal activity using medium containing 70 mM KCl, which induced a strong depolarization of the cellular membrane. The effect of this depolarization was measured in the last plot of Figure 6a, 5 min after KCl exposure. As expected, we observed that the recorded spikes were increased in amplitude as compared to the baseline. These findings demonstrated the ability of the passive electrodes to detect changes in neuronal activity upon stimulation.

Finally, our sensing platform was evaluated in the context of a pathophysiologically-relevant experiment, by assessing the impact of amyloid beta 1–42 (Aβ1-42) oligomeric species on the electrical properties of cultured neurons. Synthetic Aβ1-42 oligomers were prepared from lyophilized HFIP-treated peptide monomers (Eurogentec). Briefly, 0.5 mg of monomers were diluted in 22.15 µL of DMSO and stored at −80 °C until further use. To obtain a 100 µM stock solution, 5 µL of Aβ1-42 were diluted in 250 µL of ice-cold Neurobasal A medium minus phenol red and oligomerization was allowed to proceed by storing the preparation for 18 h at 4 °C. Such Aß1-42 oligomers have already been largely studied to better understand their toxic role in the context of Alzheimer's Disease and the consequences of their abnormal accumulation on synaptic plasticity at the cellular and network levels are well known.[34–37] This experiment was reproduced twice on different neuronal cultures at 15 DIV, using two different chips each time, with identical culture conditions and treatments, which all gave similar trends. Neurons were plated at 120 000 cells cm^{-2} and all 47 passive nano-electrodes were recorded. We conducted an experiment divided into three parts: recording of baseline activity in Tyrode solution, recording of the short-term effects of 1 µM Aβ1-42 oligomers 1 min after their addition in the medium and, finally, the effects of Aβ1-42 oligomers after at least 1.5 h of incubation with neuronal cultures. Examples of recordings of these three scenarios are presented in Figure S2 (Supporting Information), showing a more sustained activity in amplitudes after the addition of Aβ1-42 oligomers. The polarity of the recorded potentials, as shown in Figure S2 (Supporting Information), was diverse, including positive, negative, or biphasic signals, with a majority being positive. The technology captured extracellular signals without penetrating the cell membrane, thus avoiding disruption to the neuron. Scaling the electrode footprint to less than the size of an individual cell body enabled interference with sub-cellular compartments, while enhancing cell engulfment, likely reducing seal resistance (depending on overlap and distance from the cell).[38] Another aspect of our NEA technology was the nanoelectrode interface, where Pt-silicide nanoprobe surfaces provided a favorable compromise between stability and reduced impedance. Together, these efforts resulted in acquiring signals with much higher resolution. Moreover, for each case, the average current value over 100 s measured in the vicinity of the electrode in question did not evidence any pH variation during the experiment. It is worth noting that the Tyrode buffer used in these experiments did not mask the local and transient changes in proton concentration, as shown in Figure S4 (Supporting Information). In this section, small amounts of low/high pH solution (20 µL applied in less than one second) were microinjected into the vicinity of the FinFET device, inducing a rapid increase and decrease in the measured current. After spike detection, the frequency and amplitude of spikes were compiled with bar charts shown in Figure 6b,c. Recordings in real time revealed that spike frequencies increased from the baseline reference upon addition of Aβ1-42 oligomers and next decreased after the resting period (Figure 6b). This could be due to an initial acute perturbation of the neuronal culture upon addition of the oligomers, subsequently resulting in a general attenuation of the electrical activity. Moreover, the high sensitivity of this device unraveled new data, such as detecting variations in the amplitude of spikes upon incubation with Aβ1-42 oligomers, which displayed significantly different distributions as evidenced by Chi^2 test (<0.0001). Indeed, we found that the frequency of smaller spikes decreased upon addition of Aβ1-42 oligomers, consistent with the fact that these oligomers have been shown to have an influence on presynaptic calcium currents[35,36] (Figure 6c; Figure S3, Supporting Information). It could be argued that this result is in agreement with a reduction of presynaptic activity due to Aβ1-42 oligomers. It also illustrated how this setup is clearly amenable to investigate new biologically relevant topics, thanks to its remarkably high sensitivity. Importantly, in all experiments using Aβ1-42 oligomers, we simultaneously monitored potential current variations in the FinFET devices, which did not reveal any variation of pH levels upon incubation with Aβ1-42 oligomers, thereby providing further evidence that the recorded changes in the electrical properties of neurons after exposure to Aβ1-42 oligomers were likely due to synaptic events, rather than to generalized alterations of the culture milieu that would lead to changes in pH homeostasis.

3. Conclusion

Here, we presented a novel in vitro bio platform, able to perform both highly sensitive recordings of the electrical activity of primary rodent cortical neurons, while simultaneously monitoring localized evolutions of pH levels of the culture medium. This bio platform used a combination of passive vertical nanoprobes displaying a state-of-the-art level of signal resolution, with Chem-FinFETs devices with tens of milli pH sensibility. This formed a multi-sensing unit with a nanoprobe and a Chem-FinFET spatially separated by 10 µm, which was of the same order of magnitude as the size of a neuronal cell body. The sensing area was composed by an array of these multi-sensing units, allowing to probe chemically and electrically an equivalent surface of around a half mm^2. The platform was controlled by a homemade setup able to record multiplexed data in real-time from the passive electrodes and active chem-sensors. To validate its use, we conducted a neuro-relevant study to monitor the impact of Aβ1-42 oligomers on a healthy network of cortical rat neurons, which revealed a decrease of small amplitude spikes upon addition of Aβ1-42 oligomers, consistent with a likely reduction of presynaptic activity. Future studies, including the simultaneous detection of local pH variations with the electrophysiology monitoring, together with its correlation with neurodegenerative conditions could open new avenues for a better understanding of neuronal disorder mechanisms at the cellular level.

4. Experimental Section

Primary Rat Cortical Neurons—Ethics Statement: Animal handling and care for the preparation of primary neuronal cultures from rat embryos were performed in accordance with European Union Council Directive 86/609/EEC, and experiments were performed following the French national chart for ethics of animal experiments (articles R 214–87 to -90 of the "Code rural"). The protocol received approval by the local, ministry-approved, ethics committee (CEEA-122, permit number PI-U1043-DD-10). Pregnant rats were deeply anesthetized with CO_2 before euthanasia to minimize suffering.

Neurons were prepared from Sprague-Dawley rat brain embryos harvested at gestational day 17, according to Marty F et al.[39] Briefly, cortex tissue was dissected from the brains under a binocular microscope. The cortex tissue was first subjected to enzymatic dissociation in a solution of 10 U mL^{-1} papain (Worthington). Papain action was quenched with a solution (Low-ovomucoid) containing bovine serum albumin (BSA), a protease inhibitor (Trypsin inhibitor from chicken egg), and DNAse, and a gentle mechanical homogenization of the dissociated cells was performed. The cell suspension was then filtered through a 70 µm cell strainer (BD Falcon) to remove remaining clumps and centrifuged for 10 min at 1000 rpm at RT. To eliminate glial cells, cell homogenates were resuspended in neuronal medium, layered on top a 4% BSA solution diluted in neuronal medium, and centrifuged for 10 min at 1000 rpm at RT. Neuronal medium consisted of buffered Neurobasal medium, containing 2% B-27 supplement, 1.2% GlutaMAX, and 120 U: 120 µg mL^{-1} of Penicillin: Streptomycin (all from Life Technologies).

Preparation of Glial Cell-Conditioned Culture Medium: Glial cell-conditioned culture medium was prepared from the remaining tissue after isolation of the cortex using the same protocol as for neurons, minus the purification step. The resulting glial cultures were grown in culture medium containing 5% fetal calf serum for one week to favor glial cell proliferation. Once cell monolayers were obtained, the culture medium was switched to standard neuronal culture medium (i.e., serum-free culture medium) and incubated for a few days to favor release of trophic factors by the glial cell monolayer. This conditioned cell culture supernatant was next filtered through a 22 µm filter, before its use for neuronal cultures.

Preparation of pH-Adjusted Tyrode Solutions: The solution used in the experiments was based on Tyrode's salt solution (T2145) obtained from Sigma-Aldrich, with its pH adjusted using 1N HCl or 1N NaOH. The Tyrode solution was composed of specific concentrations of various salts: Calcium Chloride (anhydrous) 0.2 g L^{-1}, Magnesium Chloride (anhydrous) 0.1 g L^{-1}, Potassium Chloride 0.2 g L^{-1}, Sodium Chloride 8.0 g L^{-1}, Sodium Phosphate Monobasic (anhydrous) 0.05 g L^{-1}, and D-Glucose 1.0 g L^{-1}. This solution served the fundamental purpose of maintaining the pH and osmotic balance in the medium, while also providing essential inorganic ions and water to the cells. Before each experiment involving the transistor devices, the solutions were freshly prepared. The different pH solutions (from 6.3 to 7.5 with 0.3 steps) were obtained by adding drops of HCl or NaOH solutions in order to reach the desired pH value. During the pH calibration curves experiment, we began with the initial measurement using the lower solution (pH 6.3). Subsequently, this solution was aspirated, and devices underwent four rinses with the higher solution (pH 6.6) before proceeding to the next measurement, following this sequence iteratively.

Statistical Analysis: Pre-processing and analysis of the electrical data (acquisition, filtering, and Spike detection) are detailed in the following sections. Whenever needed (see Supporting Information), data were presented as mean ± S.E.M. Sample size was indicated in each corresponding figure. Briefly, the filtered spikes data recorded for 2 min in each condition from 60 electrodes on 2 chips were all considered. Data were analyzed by Chi^2 test or Bonferroni post-hoc tests and by repeated-measures 2-Way ANOVA as specified for each experiment. Statistical analyses were run using GraphPad Prism and Rstudio software.

Electrical Data Acquisition and Filtering: The setup enabled data recording at a rate of up to 1 million points per second, with a crosstalk suppression of −75dB. Both the multiplexer and the acquisition card were linked to a computer via a USB interface, controlled by custom LabVIEW software.

- Signal filtering from nanoelectrodes.

During data acquisition, two filtering methods could be utilized: hardware and software filtering. The multiplexer incorporated hardware filters connected in series with hardware operational amplifiers having a gain of 1. These filters restricted frequencies below 0.7 Hz and above 30 kHz. Low-frequency filtering prevented baseline drift due to static polarization, while high-frequency filtering reduced electrical background noise. After hardware filtering, the channels were connected to the acquisition card for additional processing and data recording through custom LabVIEW software. This software controlled the recording setup and conducted post-treatment on the raw measured signal. Two standard post-treatment techniques were applied to reduce noise and enhance recordings. The first method involved a moving average with a 10-data-point window, effectively reducing noise without altering signal amplitude or shape. The second method involved a high-pass filter with a 1 kHz cut-off frequency, resulting in a second-order filter. This post-treatment further enhanced signal quality.

- Signal filtering from FinFETs.

The action potentials of neurons near the transistor channel were detectable. To avoid interference with pH measurements, the signal underwent filtering to eliminate rapid signal fluctuations associated with neuronal electrical activity. We applied standard filtering via a moving average spanning 2000 data points, resulting in a 1st-order bandwidth of 4 Hz.

Spike Detection Method: Due to the large population of spike amplitude in the electrical recording, conventional fixed threshold method to identify spikes could lead to missed or false detections. To obtain better accuracy in detecting spikes while minimizing false positives, variable thresholds, which adapt to the local noise level, were implemented as the spike detection method, using MATLAB software. While the variable threshold method may overlook minor spikes, this trade-off was intentionally made to minimize the influence of background noise on the data analysis. To enhance spike detection, a criterion was incorporated that mandated a spike to be the highest point among its 500 neighboring data points. Given our 10 µs sample rate and a minimum spike duration of ≈5 ms, this criterion effectively identified genuine spikes, while reducing the risk of double-counting a single spike.

Supporting Information

Supporting Information is available from the Wiley Online Library or from the author.

Acknowledgements

This work was supported by the European Commission through the H2020 FETOPEN NEUREKA project (grant agreement number 863245) by the Region Occitanie and the University of Toulouse (INTRANEURO APR project, grant agreement number UPS 2017–411) by the LAAS-CNRS micro and nanotechnology platform, a member of the Renatech French national network. The authors thank Dr. Adrien Casanova for participating in the initial steps and for the FIB cross-section images of neurons on nanowires.

Conflict of Interest

The authors declare no conflict of interest.

Data Availability Statement

The data that support the findings of this study are available from the corresponding author upon reasonable request.

Keywords

3D nanostructures, bioelectronics, electrophysiology, nano device, neurons

Received: October 9, 2023
Revised: March 18, 2024
Published online: March 29, 2024

[1] M. E. Spira, A. Hai, *Nat. Nanotechnol.* **2013**, *8*, 83.
[2] P. Connolly, P. Clark, A. S. Curtis, J. A. Dow, C. D. Wilkinson, *Biosens. Bioelectron.* **1990**, *5*, 223.
[3] M. E. J. Obien, K. Deligkaris, T. Bullmann, D. J. Bakkum, U. Frey, *Front. Neurosci.* **2015**, *9*, 423.
[4] C. Grienberger, A. Konnerth, *Neuron* **2012**, *73*, 862.
[5] C. Grienberger, A. Giovannucci, W. Zeiger, *Nat. Rev. Methods Primers* **2022**, *2*, 67.
[6] E. J. Tehovnik, W. M. Slocum, *Neuroscience* **2013**, *245*, 179.
[7] U. Frey, U. Egert, F. Heer, S. Hafizovic, A. Hierlemann, *Biosens. Bioelectron.* **2008**, *24*, 1749.
[8] J. A. Wemmie, M. P. Price, M. J. Welsh, *Pharmacol. Rev.* **2006**, *57*, 117.
[9] M. Tresguerres, J. Buck, L. R. Levin, *Pflugers Arch.* **2010**, *460*, 405.
[10] S. M. Theparambil, P. S. Hosford, I. Ruminot, H. M. Becker, J. W. Deitmer, L. Becker, *Nat. Commun.* **2020**, *11*, 1.
[11] J. W. Deitmer, E. R. Schmidt, B. Johansson, *Front. Neurosci.* **2019**, *13*, 1301.
[12] J. A. Wemmie, J. Chen, C. C. Askwith, A. M. Hruska-Hageman, M. P. Price, B. C. Nolan, P. G. Yoder, E. Lamani, T. Hoshi, J. H. Freeman Jr., M. J. Welsh, *Neuron* **2002**, *34*, 463.
[13] A. Hai, M. E. Spira, *Lab. Chip.* **2012**, *12*, 2865.
[14] J. T. Robinson, M. Jorgolli, A. K. Shalek, M. H. Yoon, R. S. Gertner, H. Park, *Nat. Nanotechnol.* **2012**, *7*, 232.
[15] F. Santoro, S. Dasgupta, J. Schnitker, T. Auth, E. Neumann, G. Panaitov, G. Gompper, A. Offenhäusser, *ACS Nano* **2014**, *8*, 6713.
[16] A. Fendyur, N. Mazurski, J. Shappir, M. E. Spira, *Front. Neuroeng.* **2011**, *4*, 11.
[17] C. Xie, Z. Lin, L. Hanson, Y. Cui, B. Cui, *Nat. Nanotechnol.* **2012**, *7*, 174.
[18] M. Dipalo, H. Amin, L. Lovato, F. Moia, V. Caprettini, G. C. Messina, F. Tantussi, L. Berdondini, F. D. Angelis, *Nano Lett.* **2017**, *17*, 3932.
[19] Z. C. Lin, C. Xie, Y. Osakada, Y. Cui, B. Cui, *Nat. Commun.* **2014**, *5*, 3206.
[20] J. Abbott, T. Ye, L. Qin, M. Jorgolli, R. S. Gertner, D. Ham, H. Park, *Nano Lett.* **2017**, *12*, 335.
[21] J. Abbott, T. Ye, K. Krenek, R. S. Gertner, S. Ban, Y. Kim, L. Qin, W. Wu, H. Park, D. Ham, *Nat. Biomed. Eng.* **2020**, *4*, 232.
[22] R. Liu, R. Chen, A. T. Elthakeb, S. H. Lee, S. Hinckley, M. L. Khraiche, J. Scott, D. Pre, Y. Hwang, A. Tanaka, Y. G. Ro, A. K. Matsushita, X. Dai, C. Soci, S. Biesmans, A. James, J. Nogan, K. L. Jungjohann, D. V. Pete, D. B. Webb, Y. Zou, A. G. Bang, S. A. Dayeh, *Nano Lett.* **2017**, *17*, 2757.
[23] A. Casanova, L. Bettamin, M. C. Blatche, F. Mathieu, H. Martin, D. Gonzalez-Dunia, L. Nicu, G. Larrieu, *J. Phys. Condens. Matter.* **2018**, *30*, 464002.
[24] P. Shokoohimehr, B. Cepkenovic, F. Milos, J. Bednár, H. Hassani, V. Maybeck, A. Offenhäusser, *Small* **2022**, *18*, 2200053.
[25] R. Liu, J. Lee, Y. Tchoe, D. Pre, A. M. Bourhis, A. D'Antonio-Chronowska, G. Robin, S. H. Lee, Y. G. Ro, R. Vatsyayan, K. J. Tonsfeldt, L. A. Hossain, M. L. Phipps, J. Yoo, J. Nogan, J. S. Martinez, K. A. Frazer, A. G. Bang, S. A. Dayeh, *Adv. Funct. Mater.* **2022**, *32*, 2108378.
[26] J.-C. Chou, C.-Y. Weng, *Proce. of the 11th Int. Conf. Solid-State Sens. Actuators, TRANSDUCERS '01*, Munich, Germany **2001**.
[27] S. Chen, J. G. Bomer, E. T. Carlen, A. Van Den Berg, *Nano Lett.* **2011**, *11*, 2334.
[28] Y. Chen, X. Wang, M. Hong, S. Erramilli, P. Mohanty, *Sens. Actuators, B* **2008**, *133*, 478.
[29] O. Knopfmacher, A. Tarasov, W. Fu, M. Wipf, B. Niesen, M. Calame, C. Schönenberger, *Nano Lett.* **2010**, *10*, 2268.
[30] O. Knopfmacher, D. Keller, M. Calame, C. Schönenberger, *Nano Lett.* **2009**, *9*, 129.
[31] A. Casanova, M. C. Blatche, C. A. Ferre, H. Martin, D. Gonzalez-Dunia, L. Nicu, G. Larrieu, *Langmuir* **2018**, *34*, 6612.
[32] A. Gladkov, Y. Pigareva, D. Kutyina, V. Kolpakov, A. Bukatin, I. Mukhina, V. Kazantsev, A. Pimashkin, *Sci. Rep.* **2017**, *7*, 15625.
[33] S M. Theparambil, P S. Hosford, I. Ruminot, O. Kopach, J R. Reynolds, P Y. Sandoval, D A. Rusakov, L. F Barros, A V. Gourine, *Nat. Commun.* **2020**, *11*, 5073.
[34] V. Nimmrich, C. Grimm, A. Draguhn, S. Barghorn, A. Lehmann, H. Schoemaker, H. Hillen, G. Gross, U. Ebert, C. Bruehl, *J. Neurosci.* **2008**, *28*, 612.
[35] T. Yang, S. Li, H. Xu, D. M. Walsh, D. J. Selkoe, *J. Neurosci.* **2017**, *37*, 152.
[36] S. Li, M. Jin, T. Koeglsperger, N. E. Shepardson, G. M. Shankar, D. J. Selkoe, *J. Neurosci.* **2011**, *31*, 6627.
[37] F. Tamagnini, S. Scullion, J. T. Brown, A. D. Randall, *Hippocampus* **2015**, *25*, 566.
[38] M. E. Spira, N. Shmoel, S.-H. M. Huang, H. Erez, *Front. Neurosci.* **2018**, *12*, 212.
[39] F. H. Marty, L. Bettamin, A. Thouard, K. Bourgade, S. Allart, G. Larrieu, C. E. Malnou, D. Gonzalez-Dunia, E. Suberbielle, *iScience* **2021**, *25*, 103621.